



Binary junctions enhance electron storage and potential difference for photo-assisted electrocatalytic CO₂ reduction to HCOOH

Yingnan Cao^{a,c,1}, Chi Zhang^{c,1}, Wenchao Wang^{b,*}, Yunni Liu^{a,c}, Ying Tao^c, Jinchen Fan^a, Ming Chen^d, Dieqing Zhang^c, Guisheng Li^{a,c,**}

^a School of Materials and Chemistry, University of Shanghai for Science and Technology, Shanghai 200093, China

^b School of New Energy, Nanjing University of Science & Technology, Jiangyin 214443, China

^c Key Laboratory of Resource Chemistry of Ministry of Education, Shanghai Key Laboratory of Rare Earth Functional Materials, College of Chemistry and Materials Science, Shanghai Normal University, Shanghai 200234, China

^d School of Chemistry and Chemical Engineering, Yangzhou University, Yangzhou 225002, China

ARTICLE INFO

Keywords:

TiO₂
SrTiO₃
Photo-assisted electrocatalysis
Electron storage
CO₂ reduction

ABSTRACT

Photo-assisted electrocatalytic (PAEC) CO₂ conversion is a crucial approach for achieving sustainable carbon neutrality. Here, we have developed a binary-junctions photoanode by integrating SrTiO₃ and anatase-rutile TiO₂ nanotube arrays (STO/A-R TNTAs), which exhibits exceptional activity and selectivity in converting CO₂ to HCOOH. The synergetic effects of the SrTiO₃/TiO₂ heterogeneous junction and the anatase-rutile TiO₂ hetero-phase junction effectively facilitate photoelectron separation and storage, leading to a potential difference between anode and cathode. The establishment of the electron storage strategy, triggered by hetero-junction/phase interfaces, serves as remarkably efficient electron trapping regions with dam-like characteristics. As a result, the STO/A-R TNTAs achieves a generation rate of 68.24 μmol cm⁻² h⁻¹ with 92.25% selectivity and 90.70% Faradic efficiency. This performance is approximately 8 times higher compared to the pristine TiO₂ nanotube arrays photoanode. The implementation of the electron storage mechanism presents a promising approach to improve CO₂ reduction activity and selectivity.

1. Introduction

Carbon dioxide (CO₂) emission from the burning of fossil fuels has led to critical climate change. To prevent irreversible climate catastrophe and reduce CO₂ concentration in the atmosphere, it is crucial to achieve a net-zero CO₂ goal by the mid-21st century. Sustainable carbon-neutral technologies, including photocatalysis, electrocatalysis, and biotech, offer effective approaches in this regard [1–3]. CO₂, as an important carbon source, can be used to synthesize various high-value-added chemicals and fuels, such as urea, hydrocarbons (e.g., CH₄) and other molecules (e.g., CO and HCOOH) [4–8]. HCOOH, as a liquid product, has gained significant attention due to its high economic value, ease of recovery and transportation. In addition, the proton-coupled two-electron reaction pathway facilitates hydrogen storage in formic acid and other products [9,10]. Therefore, extensive efforts have been devoted to improving the catalytic performance of

proton-involved CO₂ conversion to high-value-added HCOOH from the perspective of photodynamics in the CO₂ photoreduction system [11–13]. Solid-state semiconductor-type photocatalysts play a crucial role in solar-driven CO₂ reduction due to their reasonable cost and non-toxic nature, without reliance on fossil fuel consumption and waste exportation. Compared to photocatalysis (PC) and electrocatalysis (EC), photo-assisted electrocatalysis (PAEC) shows a higher efficiency and selectivity of catalytic CO₂ reduction under extremely low working voltage (≤ 0.5 V) due to the synergistic effect of the incident photon and external bias [14,15]. In a standard photoanode-driven PAEC CO₂ conversion system, the separation of charge carriers takes place within the photoanode, subsequently leading to the transport of photo-generated electrons across the external circuit, and resulting in CO₂ reduction reaction (CO₂RR) at the cathode [16,17]. In addition, the remaining photogenerated holes on the photoanode side can be utilized to drive an oxidation reaction [18,19]. In the realm of intricate

* Corresponding author.

** Corresponding author at: School of Materials and Chemistry, University of Shanghai for Science and Technology, Shanghai 200093, China.

E-mail addresses: wenchao@njust.edu.cn (W. Wang), liguisheng@usst.edu.cn (G. Li).

¹ These authors contributed equally.

PAEC-driven CO₂ reduction, the catalytic activity and selectivity is typically influenced by two pivotal factors: 1) charge carrier dynamics (e.g. electron-hole separation, recombination and carrier migration) and 2) interfacial adsorption and activation of the target molecules (e.g. CO₂, H₂O). Significant research efforts have been dedicated to the advancement of semiconductive electrode materials, aiming to expedite charge carrier transport and augment CO₂ activation via vacancy engineering, single-atom strategy, and Z/S-scheme, as previously outlined [20–22]. Extensive studies to enhance activity of the PAEC-driven CO₂RR have been carried out in the past. One example is the implementation of a biomimetic strategy, which has demonstrated an enhanced capacity for CO₂ adsorption and conversion by effectively activating C=O bonds and facilitating C-C coupling [23]. Currently, Meyer et al. reported that the binary molecular p-n junctions can enhance the photon absorption range and generate high-energy electrons to activate CO₂ [24].

Titanium dioxide (TiO₂) is one of the most widely studied materials for photocatalysis and photo-assisted electrocatalysis applications, owing to its stability, nontoxicity and versatility [25,26]. Considerable efforts have been directed towards investigating the morphological effects on enhancing overall PAEC performance. For instance, Li et al. developed a 3D nanocone TiO₂ electrode that significantly improves mass transportation and charge transfer [27]. Moreover, 1D TiO₂ structures with rod-like and wire-like morphologies hold promise as catalysts due to the directional charge transportation and uniform anisotropy [28,29]. Compared to nanorods and nanowires, nanotube structures with unique porous channels exhibit high surface area that enhances reactant absorption and light harvesting through multiple reflection processes [30–32]. TiO₂ nanotube arrays (TNTAs) have been widely employed as n-type photoanode materials in the PAEC-driven CO₂RR. In this process, photogenerated holes migrate to the semiconductor-solution interface between TiO₂ and electrolyte to drive oxygen evolution reaction (OER), while the photogenerated electrons are transferred to the cathode side by an external bias to facilitate the CO₂RR [33]. It is important to note that for achieving highly efficient CO₂RR activity, the redox potential of photogenerated electrons needs to be more negative than that of the standard CO₂RR [34]. This requirement for a sufficiently negative potential is necessary to minimize energy losses caused by photogenerated holes passing through the space-charge region and electrons transferring through the external circuit to the counter electrode [35]. Typically, the conduction band (CB) position of TNTAs is not negative enough to provide the required driving force for highly efficient CO₂RR. Furthermore, the occurrence of ultrafast electron-hole pair recombination and photo-dynamic losses within the TNTAs photoanode imposes constraints on the overall performance of PAEC-driven CO₂RR.

Perovskite oxide SrTiO₃ has garnered significant attention due to its two potential active surfaces, namely the Sr-O and Ti-O surfaces [36]. These surfaces show a big difference in electronic and acid-base properties, with the Sr-O surface being basic and the Ti-O surface being acidic. This disparity in properties facilitates the preferential growth of alternative semiconductors. Recently, Wang et al. reported that Ti-rich SrTiO₃ demonstrates excellent performance in CO₂RR, attributed to the high density of exposed Ti ions [37]. Furthermore, the more negative flat band potential of SrTiO₃ facilitates efficient electron transfer from the CB of SrTiO₃ to that of TiO₂. The coupling of SrTiO₃ and TiO₂ in a hetero-architecture can effectively enhance charge separation, resulting in a significant improvement in catalytic performance. Although the photocatalytic properties of SrTiO₃/single-phase TiO₂ powder have been extensively investigated [38,39]. Nevertheless, the relationship between SrTiO₃ and two-phase TiO₂ (anatase and rutile) has received relatively less attention. Moreover, there is a notable lack of research on the SrTiO₃/two-phase TNTAs photoelectrode. Drawing inspiration from the water level difference-induced storage model, we propose a novel approach to enhance the storage and utilization of photoelectrons in the PAEC system. This approach enables the efficient storage of electrons and the elevation of energy levels, thereby facilitating the generation of

high-energy electrons. However, the driving force for the STO/single-phase TNTAs heterogeneous junction remains insufficient, as the electron potential is prone to loss from the single component. One viable approach to achieve a more negative electron potential is to tune the band-edge position and construct a channel resembling a dam structure. Inspired by the phase transformation of TNTAs, the anatase (A) and rutile (R) phases show different band edge positions, which can easily form an effective electron storage and potential elevation through an *in-situ* heterophase junction. Theoretically, due to the more positive CB position than that of (A) TNTAs, (R) TNTAs can act as an effective dam-like site to store and elevate the electron potential in SrTiO₃/two-phase TNTAs photoelectrode. Therefore, it may be a successful strategy to introduce the binary junctions to improve active electrons storage and potential difference.

Here, a photoanode featuring binary junctions (heterogeneous and heterophase) between SrTiO₃ (STO) and anatase-rutile TNTAs (A-R TNTAs) was synthesized with the aim of enhancing electron storage for highly efficient CO₂RR. To facilitate PAEC-driven CO₂ reduction to HCOOH, a copper foam, widely investigated for this purpose, was employed as the cathode. The disparate band edge positions of TiO₂ (anatase phase), TiO₂ (rutile phase), and SrTiO₃ facilitated the interfacial electron transfer and storage, thereby elevating the potential of photoexcited electrons and extending their effective lifetimes. By harnessing the electron storage capability inherent in the photoanode, the fabricated PAEC cell exhibited outstanding performance in CO₂RR, resulting in a remarkable production rate of 68.24 μmol cm⁻² h⁻¹ of HCOOH (with a selectivity of 92.25% and a Faradic efficiency of 90.7%). This yield was approximately 8 times higher compared to using pristine TNTAs and STO as the photoanode, respectively.

2. Experimental section

2.1. Preparation of TiO₂ nanotube arrays

The highly ordered vertical TiO₂ nanotube arrays (TNTAs) were prepared by versatile anodic oxidation. The polished titanium sheet (0.3 mm thick, 99.5%, purchased from Shanghai Right Titanium Industry Co., Ltd.) was cut into small pieces with a size of 33 * 20 * 0.3 mm. Then the titanium foils were ultrasonically cleaned in acetone (Aladdin Co., Ltd. 99.9%), ethanol (Aladdin Co., Ltd. 99.9%) and deionized water for 15 min, respectively. The cleaned titanium foils were anodized at a constant potential of DC 20 V in an aqueous solution, which contained 30 mL H₃PO₄ (0.2 M, Aladdin Co., Ltd.) and 30 mL NH₄F (0.4 M, Aladdin Co., Ltd.), for 7 h in a two-electrode setup with a Pt (20 * 20 * 0.2 mm, 99.99%) as the cathode under DC constant voltage power. After anodic oxidation, the samples were rinsed with water and ethanol, respectively. The rinsed samples were further dried and calcined in a muffle furnace at 450 °C (5 °C/min) for 2 h in the air to obtain TiO₂ nanotube arrays.

2.2. Preparation of STO/A-R TNTAs

In a typical process, the STO/A-R TNTAs photoanode was fabricated by a hydrothermal method. Two pieces of TNTAs films were immersed in 50 mL Sr(OH)₂·8 H₂O (0.04 M, Aladdin Co., Ltd. 99.995%) aqueous solution in a 100 mL Teflon-lined stainless steel autoclave. After hydrothermal reaction at 150 °C for 10 h, the as-obtained films were taken out and washed with 0.1 M hydrochloric acid (Aladdin Co., Ltd. 37.8%), rinsed with deionized water three times and dried in an oven at 40 °C for further treatment. To increase the crystallinity of SrTiO₃ and the interaction between SrTiO₃ and TNTAs, the as-formed films were further calcined at different temperatures (450, 600 and 750 °C), and the corresponding samples are described as SrTiO₃/anatase TiO₂ (STO/A TNTAs), SrTiO₃/anatase-rutile TiO₂ (STO/A-R TNTAs) and SrTiO₃/rutile TiO₂ (STO/R TNTAs), respectively.

2.3. Preparation of SrTiO₃ powder

As a reference, SrTiO₃ powders were also prepared by a hydrothermal route. 10 mL commercial tetrabutyl titanate and 8.0 g Sr(OH)₂·8 H₂O were dispersed in 40 mL distilled water. Subsequently, the mixture was transferred to a 50 mL Teflon-lined autoclaves followed by hydrothermal treatment at 150 °C for 10 h. White powders were centrifuged, washed with deionized water several times and dried at 40 °C in the air. The as-prepared powders were further calcined at 600 °C for 2 h in the air for further utilization.

2.4. Characterizations

X-ray diffraction measurements were carried out in parallel mode (2θ varied from 10 to 80 °) using a Rigaku Dmax-3 C Advance X-ray diffractometer (Cu Kα radiation, λ = 1.5406 Å). Scanning electron microscopy (SEM) images were obtained using a JEOL JSM-6380LV. High-resolution transmission electronic microscopy (HRTEM) images, EDX mapping images and the selected area electron diffraction (SAED) images were all collected on a JEM-2010 instrument. The UV–vis diffuse reflectance spectra (UV–vis DRS) were obtained using a MC-2530 instrument. The surface electronic states were analyzed by X-ray photoelectron spectroscopy (XPS, Perkin-Elmer PHI 5000). All the binding energy values were calibrated using C1s = 284.8 eV as a reference. UPS spectra were measured using He I excitation (21.2 eV) and recorded with a constant pass energy of 5 eV in the ultrahigh vacuum (UHV) chamber of the XPS instrument. UPS binding energies were referenced to the Fermi edge, which was sputtered onto the sample (W = 3000 eV, Area = 2.0 mm) in the UPS chamber for 50 s at −10 eV. Incident-photon-to-current conversion efficiency (IPCE) measurements were performed in a standard three-electrode system by using the electrochemical workstation (ZAHNER-Elektrik), with the applied potential of 0.5 V vs. Ag/AgCl and the light source wavelength from 367 to 720 nm. The ns-TA experiments were conducted with a commercial instrument, LP920 laser flash spectrometer (Edinburgh Instruments). The 355 nm pump laser pulse was generated by the third harmonic output of an Nd: YAG laser. IPCE is generally defined as the number of photo-generated charge carriers contributing to the photocurrent per incident photon. It can be calculated based on the following equation [40]:

$$\text{IPCE} = \frac{\text{total energy of converted electrons}}{\text{total energy of incident photons}} = \frac{\left(\frac{J_{\text{photo}}(\lambda)}{e}\right) \left(\frac{hc}{\lambda}\right)}{P(\lambda)}$$

where $J_{\text{photo}}(\lambda)$ is the photocurrent density at that particular wavelength of incident light (nm); $P(\lambda)$ is the incident light intensity (mW cm^{−2}); e is the charge of an electron (1.602×10^{−19} C); h is Planck's constant (6.626×10^{−34} J s); c is the speed of light (3.0×10⁸×10⁹ m s^{−1}); λ is the specific wavelength (mW cm^{−2}).

2.5. Photo-assisted electrocatalytic CO₂ reduction measurement

The photo-assisted electrocatalytic reduction of CO₂ was carried out in an H-type cell reactor (100 mL per chamber) on an electrochemical station (CHI 660E), with the as-prepared STO/A-R TNTAs photoanode as the working electrode, copper foam (30 × 20 × 1.0 mm) as the counter electrode and Ag/AgCl as the reference electrode. Before the reaction, 60 mL Na₂SO₄ (0.5 M) as the electrolyte in the cathode chamber was purged with high-purity CO₂ (99.999%) gas for 30 min. In the anode chamber, high-purity N₂ (99.999%) was bubbled for 30 min to remove the dissolved oxygen. A Xe lamp (300 W, 1240 mW cm^{−2}) was employed as the light source and positioned 10 cm away from the photo-induced electrochemical cell. The operation of photo-induced electrocatalytic H₂ evolution test was similar to CO₂ reduction but the cathode was changed to Pt foil purged with high purity N₂ (99.999%). To quantify the amount of the evolved H₂, 0.5 mL of the gas was sampled

intermittently through the septum after 1 h of reaction and was analyzed by gas chromatography (GC-2002, Shanghai Ke Chuang Chromatograph Instruments Co. Ltd., China, TCD detector, with N₂ (99.999%) as the carrier gas with TDX-1 columns). The liquid product of HCOOH was detected by ion chromatography (ICS-5000, IonPacAS11-HC, 4×250 mm, Dionex IonPac AS19-4 μm Analytical Column (4×250 mm), Dionex IonPac AS19-4 μm Guard Column (4×50 mm).

3. Results and discussion

3.1. STO/A-R TNTAs photoelectrode characterizations

As described in Fig. 1a, the STO/A-R TNTAs binary junctions photoanode was fabricated via two steps. Firstly, highly ordered vertical anatase TNTAs were *in-situ* synthesized using an anodic oxidation approach, followed by calcination for crystallization. The as-obtained TNTAs were further hydrothermally treated in an aqueous solution containing Sr(OH)₂·8 H₂O precursor to form the heterogeneous STO/TNTAs heterogeneous. The formed STO/TNTAs film was further calcined at 600 °C to enhance the interaction between SrTiO₃ and TNTAs and form a SrTiO₃/anatase-rutile TiO₂ nanotube arrays (STO/A-R TNTAs) photoanode. Scanning electron microscopy (SEM) was employed to examine the morphologies of the pristine TNTAs as well as the STO/A-R TNTAs samples. After subjecting the pristine TNTAs to a 7 h anodic oxidation process, the average length of the nanotubes was determined to be approximately 1.41 μm, as shown in Figure S1a and Figure S2b. Following the incorporation of SrTiO₃ particles, the diameter and surface roughness of the STO/TNTAs were both observed to undergo an increase. (Figure S1b). X-ray diffraction (XRD) patterns were employed to elucidate the chemical composition and phase structure of the as-synthesized electrodes. (Fig. 1b). All the samples demonstrated the characteristic anatase crystal phase (red, JCPDS No. 21–1272) of TNTAs [41]. The STO/TNTAs sample, which did not undergo annealing treatment, exhibited weak diffraction peaks, indicating the inferior crystallinity of the as-synthesized SrTiO₃ and the limited interaction between TiO₂ and SrTiO₃. The intensities of the SrTiO₃ (110) characteristic peak at 32.2° (blue, JCPDS No. 35-0734) were observed to significantly increase with the elevation of annealing temperature [42]. Additionally, it should be noted that the weak diffraction peaks detected at 36.5° and 63.2° can be attributed to the (101) and (002) crystal planes of rutile TiO₂. (green, JCPDS No. 21-2176). The contents of the anatase and rutile phase were calculated by using the following formula [43]:

$$X_a = 1 / \left(1 + 1.26 \times \frac{I_r}{I_a} \right) \quad (1)$$

where X_a refers to the weight fraction of anatase in the mixture, I_a and I_r are the intensities of anatase (101) and rutile (110) diffraction peaks, respectively. Upon calcination at 600 °C, it was observed that a portion of the anatase phase underwent transformation into the rutile phase, and approximately 81.5% of the anatase phase was converted into rutile after calcination at 750 °C. In order to gain deeper insights into the robust interaction between STO and TNTAs in the STO/A-R TNTAs sample, X-ray photoelectron spectroscopy (XPS) was employed to analyze the binding energy shifts of Ti 2p_{3/2} and Sr 3d. As illustrated in Fig. 1c, the Sr 3d spectrum was subjected to fitting utilizing two distinct doublets, displaying a spin-orbit splitting of approximately 1.8 eV between 3d_{5/2} and 3d_{3/2}. The initial prominent doublet was observed at 133.3 and 135.1 eV, which corresponded to the characteristic peaks associated with SrTiO₃ [44]. The second doublet was observed at lower binding energies, specifically at 134.2 and 132.4 eV, and can be attributed to SrO.[45] Additionally, the Ti 2p_{1/2} and Ti 2p_{3/2} peaks exhibited characteristic binding energies of 464.6 and 458.9 eV, respectively (Fig. 1d) [46]. Significantly, smaller fractions displaying lower binding energies (463.5 and 457.9 eV for Ti³⁺ species) were also identified. To better understand the changes in the chemical

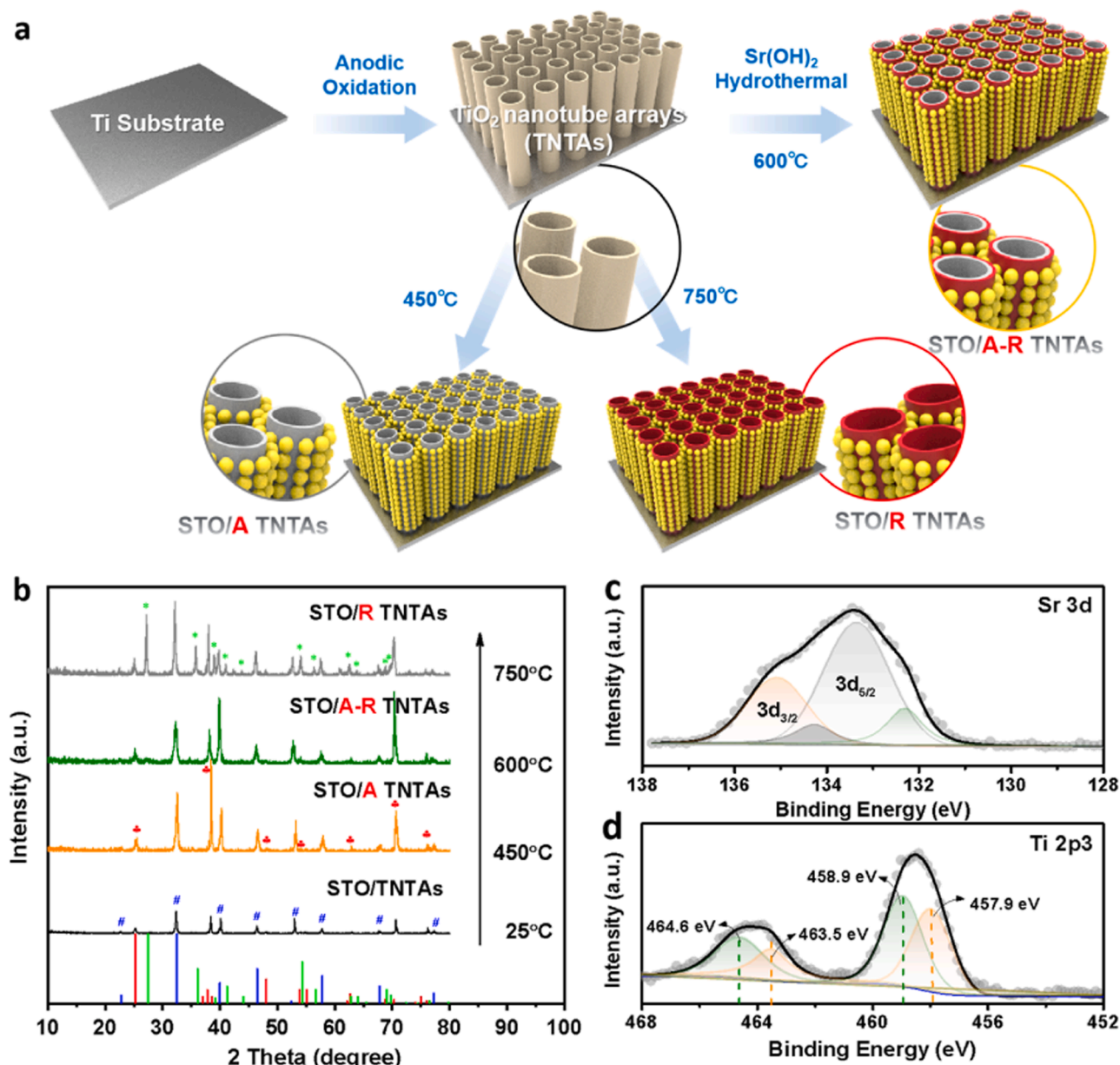


Fig. 1. (a) Schematic of the synthesis of STO/A-R TNTAs photoanode; (b) XRD patterns of (black line) STO/TNTAs without annealing treatment, (orange line) STO/A TNTAs, (green line) STO/A-R TNTAs and (gray line) STO/R TNTAs, respectively; high-resolution XPS spectra of (c) Sr 3d and (d) Ti 2p3 of STO/A-R TNTAs sample.

environment before and after the formation of the STO/A-R TNTAs hybrid, high-resolution XPS of bare Sr 3d in STO and Ti 2p in TiO₂ were conducted for comparison (Figure S3). The pure SrTiO₃ sample exhibits a higher binding energy (134.7 and 133.0 eV) than that of STO/A-R TNTAs (Figure S3a). However, a slight blue shift of Ti³⁺ species is observed in the TNTAs, indicating the new chemical interaction between the internal Sr of SrTiO₃ and the external Ti of TNTAs.

To verify the crystal structure of the as-synthesized STO/A-R TNTAs, STO/A-R TNTAs layers were removed from Ti foil via ultrasonication and subsequently characterized through transmission electron microscopy (TEM). As shown in Fig. 2c, STO/A-R TNTAs exhibit a large ordered porous structure with an average pore size of about 50 nm, which is smaller than that of pure TiO₂ nanotubes. Furthermore, the STO/A TNTAs sample exhibits a comparable porous structure to that of the STO/A-R TNTAs (Fig. 2a). This phenomenon can be attributed to the potential presence of STO layers enveloping the inner or outer surface of the TiO₂ nanotubes. The corresponding selected area electron diffraction (SAED) pattern of the STO/A TNTAs was also performed, as shown

in Fig. 2b. The image at the bottom shows the ring radius of STO (blue) and anatase (red). The crystal planes of (113), (013), (022), (112), (002), and (011) are ascribed to typical SrTiO₃ crystal, while (004), (011) are ascribed to the anatase phase of TiO₂. Upon being calcined at 600°C (STO/A-R TNTAs), the main (113) crystal plane of STO disappeared, and (151), (141) crystal planes were observed due to the formation of the rutile phase of TiO₂ (Fig. 2d).

The high-resolution transmission electron microscopy (HRTEM) image of STO/A-R TNTAs reveals notable characteristic lattice spacing of both STO and TiO₂, as shown in Fig. 2e. Specifically, the lattice fringe of 0.225 nm corresponds to the (111) plane of STO, while the lattice fringes of 0.249 nm and 0.325 nm match well with the (101) and (110) planes of rutile TiO₂, respectively [47,48]. Moreover, two sets of lattice fringes with 0.352 nm and 0.233 nm can be ascribed to the (101) and (112) planes of anatase [49]. The HRTEM analysis indicates that rutile islands are surrounded by STO layers (circled by the red line in Fig. 2e) and form at the interface between STO and anatase TiO₂. HAADF-STEM and EDX elemental mapping were used to analyze the distribution of

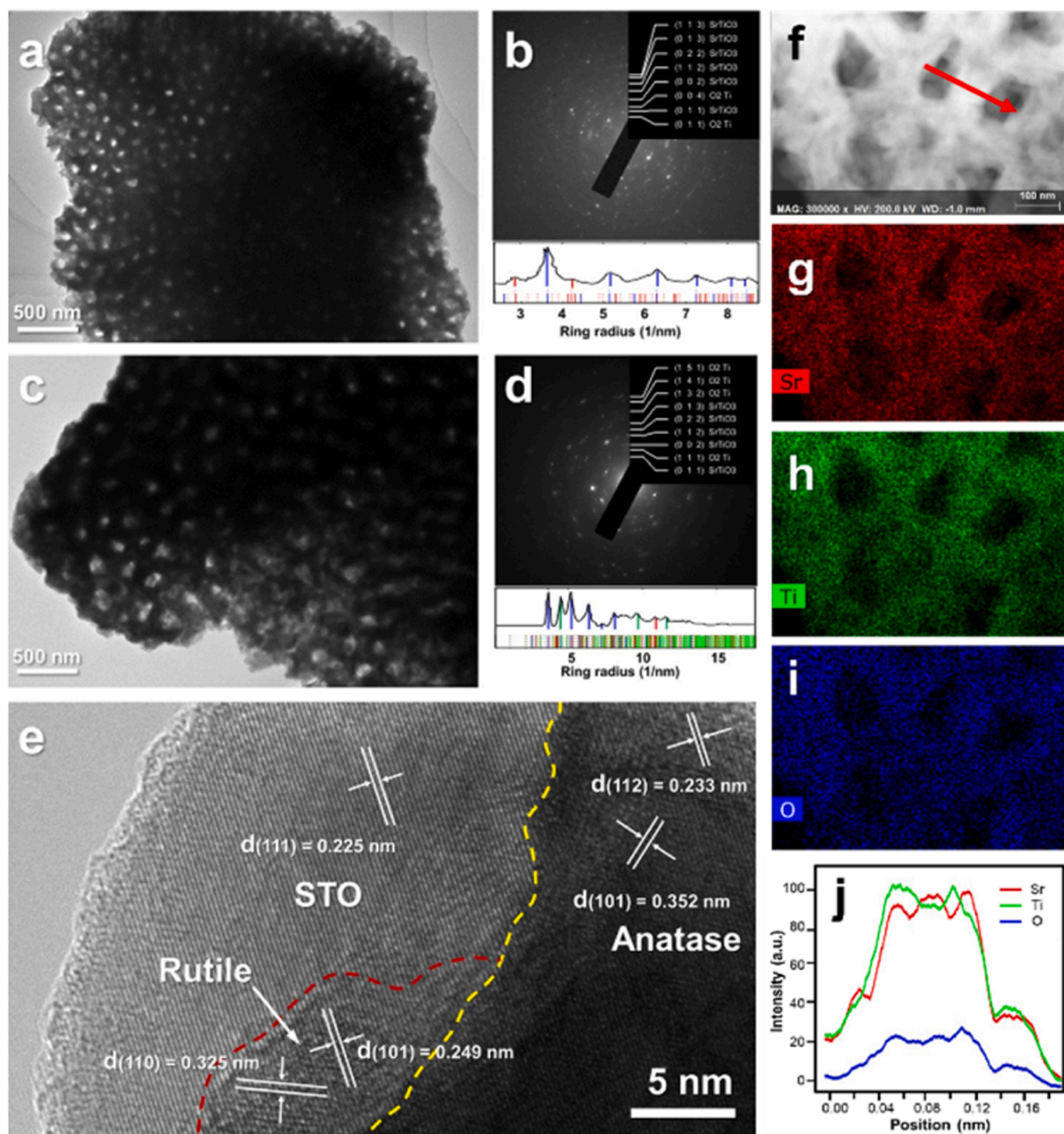


Fig. 2. (a) TEM image and (b) the corresponding SAED patterns of STO/A TNTAs; (c) TEM image and (d) the corresponding SAED patterns of STO/A-R TNTAs; (e) HRTEM image of STO/A-R TNTAs, (f-i) HAADF-STEM and STEM-EDX elemental mapping images of STO/A-R TNTAs, and (j) Line-scanning profiles of Sr, O, and Ti along the center of two nanotubes from the (f).

elemental compositions (Fig. 2f-i). It is observed that the elements of Sr, O and Ti are uniformly dispersed on the surface of the nanotubes pore walls. Line-scanning profiles along the center of two nanotubes of STO/A-R TNTAs were also conducted to investigate the distribution of STO layers. As illustrated in Fig. 2j, the TiO₂ nanotube walls were evenly coated with STO layers. The collective findings indicate the successful formation of binary junctions in the form of one-dimensional vertical STO/A-R TNTAs. The larger surface area and better utilization ratio of

light in STO/A-R TNTAs are expected to enhance their photon absorption capacity. Additionally, the one-dimensional structure with a high degree of crystallization can facilitate electron transport and minimize photodynamic loss at binary junctions [30]. Hence, it can be anticipated that the nanotube arrays comprising the synthesized STO/A-R TNTAs possess the potential to function as a proficient photoanode for facilitating the PAEC-driven CO₂RR.

3.2. Photo-assisted electrocatalytic CO₂RR performance measurements

The performance of the photo-assisted electrolysis cell (PAEC)-driven CO₂RR was assessed through a three-electrode H-type cell configuration (Figure S4). The setup was composed of an STO/A-R TNTAs photoanode (serving as the working electrode), a Cu foam cathode (acting as the counter electrode), and an Ag/AgCl reference electrode. The photo-generated electrons were conveyed from the anode to the cathode through the external circuit, wherein the performance of both CO₂RR and hydrogen (H₂) production were evaluated. The primary outcome of the CO₂RR was determined via gas chromatography and ion chromatography analysis, which indicated that the primary product was HCOOH, while H₂ was produced as a secondary product. As shown in Fig. 3a, both pristine TNTAs and STO exhibited a very low HCOOH production rate of approximately 8.3 $\mu\text{mol cm}^{-2} \text{h}^{-1}$. Importantly, coating STO layers on the wall of TNTAs for the STO/A TNTAs sample led to a significant increase in the HCOOH production rate, reaching 39.1 $\mu\text{mol cm}^{-2} \text{h}^{-1}$. Moreover, an increase in the calcination temperature to 600 °C for STO/A-R TNTAs resulted in a substantial augmentation of the HCOOH production rate, which reached 68.2 $\mu\text{mol cm}^{-2} \text{h}^{-1}$. This demonstrated a 174% improvement in comparison to STO/A TNTAs and an 800% enhancement in comparison to TNTAs. However, the HCOOH production rate for STO/R TNTAs significantly decreased to 27.9 $\mu\text{mol cm}^{-2} \text{h}^{-1}$ after being calcined at 750 °C, which can be attributed to the phase transformation to rutile. In comparison to STO/R TNTAs, the higher PAEC activity observed for STO/A TNTAs may be attributed to its slower charge recombination rate, higher charge carrier mobility, and deeper excitation of charge carriers in bulk rutile TiO₂ [50]. The detection of H₂ evolution at the cathode implies that a fraction of the photo-generated electrons on the copper foam electrode were utilized for the reduction of protons. The selectivity for CO₂RR can be calculated using the following equation [51]:

$$\text{Selectivity (\%)} = \frac{\text{moles of HCOOH}}{\text{total moles (HCOOH + H}_2\text{)}} \times 100 \quad (2)$$

As listed in Table S1, a product selectivity of 59.65% for HCOOH from CO₂RR was achieved over the TNTAs photoanode. The pristine STO photoanode exhibited remarkable selectivity of 97.85%, albeit with a relatively low rate of HCOOH production rate. This observation suggests that the STO photoanode effectively suppresses H₂ generation while facilitating the reduction of CO₂ to formic acid. Conversely, the STO/A-R TNTAs sample displayed superior HCOOH production with a rate of 68.2 $\mu\text{mol cm}^{-2} \text{h}^{-1}$ and a commendable selectivity of 92.25%. The molecular structure of potential liquid products was further examined using 1 H nuclear magnetic resonance (1 H NMR) analysis after a one-day reaction (Figure S5). Significantly, two characteristic peaks at 8.01 and 11.07 ppm can be ascribed to the specific hydrogen in the carbonyl and hydroxyl groups, respectively. Moreover, no additional impurity peaks were detected, demonstrating the high selectivity of the PAEC-driven CO₂RR towards formic acid production.

To optimize the performance of PAEC-driven CO₂RR, various conditions were investigated, including the precursor concentration, anodization time, and applied bias potential. The effects of each of these parameters were analyzed and are presented in Figure S6. The optimum CO₂RR performance was attained when utilizing a Sr(OH)₂ concentration of 0.04 M. Varying anodization times were employed to regulate the length of TiO₂ nanotubes. It was observed that the length of the TiO₂ nanotube photoanode exerted a notable impact on the performance of PAEC-driven CO₂RR. TiO₂ nanotubes of shorter length were found to diminish the transmission path of photogenerated electrons, albeit at the cost of reduced efficiency in electron and hole pair separation. Conversely, TiO₂ nanotubes of longer length exhibited the opposite trend. Notably, an anodization time of 7 hours, resulting in a suitable length of TiO₂ nanotubes (~1.41 μm), exhibited the highest HCOOH production rate. In addition, the PAEC-driven CO₂RR activities were investigated under different working potentials, ranging from 0.3 to

0.6 V (vs. Ag/AgCl). Figure S6c shows that the production rate of HCOOH increased from 38.16 to 68.24 $\mu\text{mol cm}^{-2} \text{h}^{-1}$ when the applied bias potential was changed from 0.3 to 0.5 V. However, subsequent to exceeding the working potential of 0.6 V, a diminution in CO₂RR activity was observed. This outcome could be attributed to the escalated utilization of electrons towards the reduction of water into H₂ at higher working potentials.

The photocurrent response of STO/A-R TNTAs (Figure S6d) was examined under solar light irradiation. The intensity of the photocurrent exhibited a continuous increase as the applied potential was raised. To enhance the performance of CO₂RR and mitigate the evolution of H₂, a working potential of 0.5 V (vs. Ag/AgCl) was selected, taking into account the concurrent reaction of hydrogen generation and the requirement for an optimal photocurrent. As shown in Figure S6e, both electrocatalysis (EC) and photocatalysis (PC) were employed as reference methods to accentuate the exceptional performance of photo-assisted electrocatalytic CO₂RR. The HCOOH production rate of PAEC showed approximately 600–700% enhancement compared to the reference catalysts. These results demonstrate the advantage of PAEC-driven CO₂RR with ultrafast charge carrier separation efficiency. To investigate the durability of the STO/A-R TNTAs photoanode for continuous conversion of CO₂ to HCOOH, a long-term photocurrent density test was conducted, as shown in Figure S8a. Notably, it exhibited a steady photocurrent platform under simulated sunlight irradiation during the 24-hour measurement, demonstrating sustainable CO₂RR [52]. Furthermore, the morphology of the STO/A-R TNTAs photoanode was investigated using high-resolution TEM images (Figure S8b-c). The existence of stable binary junctions provides additional evidence for the enduring operational potential of the STO/A-R TNTAs photoelectrode. The selectivity and efficiency of CO₂RR driven by PAEC method using the STO/A-R TNTAs photoelectrode are highly comparable to numerous other catalysts documented in the literature, as summarized in Table S2. Significantly, the STO/A-R TNTAs demonstrate superior Faradaic efficiency and selectivity when compared to other reported catalysts. This highlights the promising practical application potential of the STO/A-R TNTAs photoelectrode for the conversion of CO₂ into high-value-added product (HCOOH).

To obtain a more comprehensive understanding of the PAEC-driven CO₂RR over the STO/A-R TNTAs sample, the pertinent photoelectronic properties were examined and are presented in Fig. 3. Notably, the photocurrent response intensity of STO/A-R TNTAs was much lower than that of STO/A TNTAs in both the photocurrent response (Fig. 3b) and LSV curves (Fig. 3d), while STO/A-R TNTAs showed a higher HCOOH production rate (Fig. 3a). It is well known that a high photocurrent intensity is favorable for superior photocatalysis. Therefore, we propose that the photogenerated electrons in the STO/A TNTAs sample may be used to reduce protons for H₂ evolution. As proven in Fig. 3c, STO/A TNTAs indeed show the highest H₂ evolution rate under light irradiation. These results indicate that the photogenerated electrons of the as-prepared TNTAs-based photoanodes could be selectively tuned for CO₂RR or H₂ evolution via contrasting different built-in junctions. The performance of oxygen evolution over TNTAs, STO/A TNTAs, STO/R TNTAs, and STO/A-R TNTAs photoanodes were evaluated (Figure S7). Compared to the STO-modified single-phase TNTAs samples, STO/A-R TNTAs exhibited the highest OER performance due to the robust electron-hole separation achieved by constructing binary junctions. The more positive VB positions of (A) and (R) TNTAs promote hole transfer to STO before recombination with free electrons. The highest rate of oxygen (O₂) production achieved by the STO/A-R TNTAs photoelectrode is 8.71 $\mu\text{mol cm}^{-2} \text{h}^{-1}$, surpassing the rates observed with STO-modified single-phase TNTAs (2.28 $\mu\text{mol cm}^{-2} \text{h}^{-1}$ for STO/A TNTAs and 1.20 $\mu\text{mol cm}^{-2} \text{h}^{-1}$ for STO/R TNTAs) by 3.8 and 7.2 times.

Mott-Schottky (MS) measurements were performed to analyze the photogenerated carrier concentrations of the photoanode and to investigate the impact of the interfacial interaction between the photoanode and the electrolyte. (Fig. 3e-g). As the Fermi level of the semiconductor

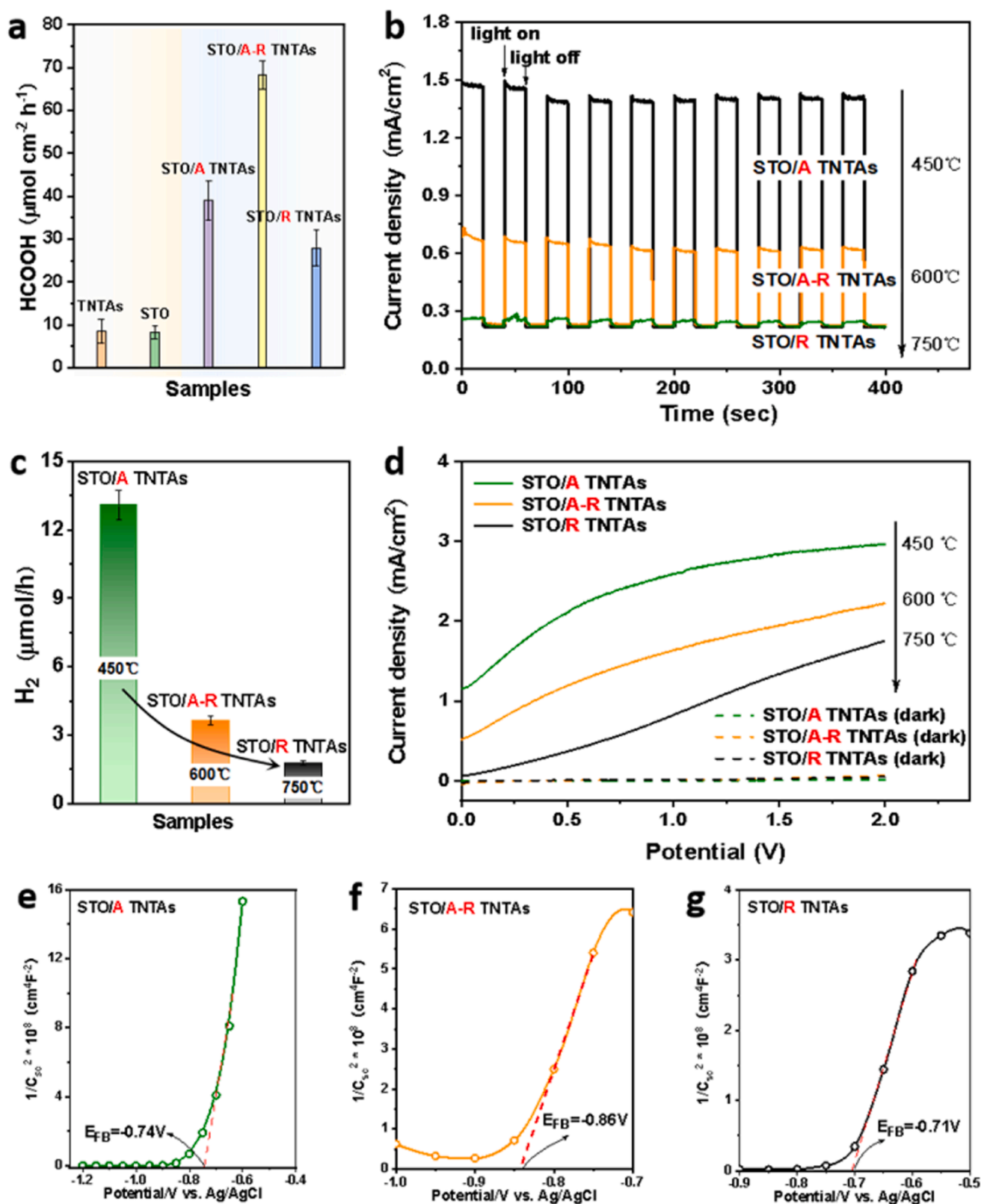


Fig. 3. (a) PAEC-driven HCOOH production rate from CO₂ by using pristine TNTAs, SrTiO₃, STO/A TNTAs, STO/A-R TNTAs and STO/R TNTAs, respectively, as the photoanode under a 300 W Xe-lamp illumination; (b) Photocurrent-time (i-t) curves of STO/A TNTAs, STO/A-R TNTAs and STO/R TNTAs under illumination and dark conditions at a constant potential of 0.5 V (vs. Ag/AgCl); (c) The H₂ evolution rate of STO/A TNTAs, STO/A-R TNTAs and STO/R TNTAs under 300 W Xe-lamp illumination. (d) Current density-potential characteristics for STO/A TNTAs, STO/A-R TNTAs and STO/R TNTAs under illumination and dark conditions; Mott-Schottky plots of (e) STO/A TNTAs; (f) STO/A-R TNTAs; (g) STO/R TNTAs measured in an aqueous solution of Na₂SO₄ (0.5 M).

shifts to the equilibrium state, the valence and conduction band energies will also shift near the semiconductor-electrolyte interface, resulting in a certain degree of upward band bending [53,54]. The flat band potential is defined as the applied voltage that allows the band positions of the conduction band (CB) and valence band (VB) to reach flat state. For n-type semiconductors, this condition typically occurs in the negative voltage range. Therefore, the E_{fb} values represent the extent of band bending in the semiconductors, from which the positions of the CB and VB band edges of various STO/TNTAs photoanodes can be calculated. In the MS plots, the positive slopes indicate the n-type characteristic of all the as-prepared TNTAs-based photoanodes. The E_{fb} values for STO/A TNTAs, STO/A-R TNTAs, and STO/R TNTAs are estimated to be approximately -0.74 , -0.86 , and -0.71 V vs. Ag/AgCl, respectively, or -0.54 , -0.66 , and -0.51 V vs. RHE at $1/C^2 = 0$. From the plots, it can be observed that the flat band potential of STO/A-R TNTAs is more negative than that of both STO/A TNTAs and STO/R TNTAs, indicating the most pronounced band bending extent and the highest equilibrium CB position. This observation could be related to the results of the HCOOH production rate. Thus, the PAEC-driven CO_2RR activity may depend on the equilibrium CB position of the photoanode.

3.3. Photo-assisted electrocatalytic CO_2RR mechanism

The UV-vis diffuse reflectance spectrum (UV-DRS) was carried out to identify the optical absorption properties and band structures of each sample. As shown in Figure S9, the band gap of STO/A-R TNTAs is calculated to be 3.28 eV based on the Kubelka-Munk function [55]. The maximal VB position (3.08 eV) of STO/A-R TNTAs is estimated from UPS analysis as shown in Figure S10. Fig. 4 shows the energy diagram and band alignment of STO/A TNTAs, STO/A-R TNTAs and STO/R TNTAs sample in quasi-static equilibrium under illumination conditions. The absorption of photons by photoanode generates a photopotential, splitting the Fermi level to $E_{F,h+}$ for the hole and $E_{F,e-}$ for the electron, leading to oxidation reactions on the VB and reduction reactions on the CB throughout the bulk semiconductor [40]. This leads to upward band bending and the formation of a depletion region at the solid-liquid interface. Applying a positive bias enhances polarization of the STO/A-R TNTAs, increasing upward bending and facilitating separation and transfer of photogenerated electrons and holes. The electron quasi-Fermi level ($E_{F,e-}$) can be estimated based on the flat band value (qV_{fb}), representing electron energy transfer to the cathode side in the closed-loop circuit of a photoelectrochemical (PAEC) system [56]. It is

challenging to generate photoelectrons with high energy to supply enough over-potential for CO_2 reduction to various products. By achieving the highest equilibrium CB potential, triphasic STO/A-R TNTAs outperform biphasic STO/A TNTAs and STO/R TNTAs, providing higher overpotential to overcome CO_2 reduction barriers. Furthermore, to obtain the relationship between light absorption and the photo-induced electrocatalytic activities of TNTAs-based photoanodes, incident-photon-to-current conversion efficiency (IPCE) measurements were performed at 0.5 V vs. Ag/AgCl under light irradiation (Figure S11). Compared with STO/A TNTAs (0.26%) and STO/R TNTAs (0.19%), STO/A-R TNTAs exhibits a highest photo-electron conversion efficiency (0.45%) at 400 nm, indicating that the electron-traps in STO/A-R TNTAs greatly enhance both the separation and utilization efficiency of photogenerated charge carriers.

A possible mechanism of PAEC-driven CO_2RR is proposed, as shown in Fig. 5a. The heterogeneous junction formed between STO and anatase TiO_2 (or rutile TiO_2) serves as a pathway for the transfer of photo-generated electrons from a high potential position to a low potential position. Fig. 5a illustrates the model of the STO/A-R TNTAs binary junction structure for the CB position. In the STO/A TNTAs sample, the photogenerated electrons on STO can directly transfer to the CB of anatase TiO_2 and then flow to the copper foam cathode through an external circuit. An electron storage process occurs from both STO and (A) TNTAs to (R) TNTAs to store and elevate the potential of the photogenerated electrons, leading to the improvement of potential difference between anode and cathode for high energy electron-involved CO_2RR to HCOOH. The electrostatic potential of $SrTiO_3$, anatase TiO_2 , and rutile TiO_2 was determined through theoretical calculations using the GGA-PBE function. Fig. 5b shows that both anatase and rutile TiO_2 have a higher electrostatic potential compared to $SrTiO_3$. The average potential of $SrTiO_3$ is -10.36 eV, while it is -5.05 and -5.85 eV for rutile and anatase, respectively. Consequently, an outward vector of E_{in} is established at the $SrTiO_3$ /anatase and anatase/rutile interfaces. This potential shift is consistent with the electron storage mechanism, which arises from the fundamental difference between $SrTiO_3$ and anatase/rutile TiO_2 . In STO/A-R TNTAs, this oriented E_{in} governs the directional charge transfer, finally storing the photogenerated electrons of $SrTiO_3$ and anatase TiO_2 at rutile TiO_2 . Experimental analysis and DFT calculations have demonstrated that the formation of STO/A-R binary junctions effectively enhances electron-hole separation and active electron transfer for CO_2RR , as shown in Scheme 1.

In addition, the presence of the electron storage mechanism in STO/A-R TNTAs junctions results in a prolonged lifetime of photogenerated electrons. The amperometric $i-t$ curves of these photoanodes under chopped-light irradiation are investigated to illustrate the lifetime of photogenerated electrons (Fig. 5c). It was observed that the photocurrent decay time for STO/A-R TNTAs was 5.0 s before reaching a steady-state, which is significantly longer compared to STO/A TNTAs (2.2 s) and STO/R TNTAs (0.2 s). This prolonged decay time can be attributed to the high-frequency occurrence of electron storage and the enhanced potential difference in the binary junctions. Moreover, the lifetime of electrons (τ_e) was calculated using the equation derived from the Bode phase plots of EIS spectra, as illustrated in Fig. 5d [57]:

$$\tau_e = 1/\omega_{max} = 1/(2\pi f_{max}) \quad (5)$$

where f_{max} is the maximum frequency for the medium frequency peak. The lifetime of the photogenerated electrons in STO/A-R TNTAs is calculated to be 1500 ns, which is approximately 2.0 times higher than that of STO/A TNTAs and STO/R TNTAs (Figure S12). The nanosecond photoluminescence (ns-PL) decay (Figure S13) and the corresponding exponential function fitting (Table S3) reflect the excited-state lifetime and charge carrier recombination process. Generally, an increased PL lifetime indicates a longer excited-state lifetime, which results from the effective suppression of photo-generated electron-hole pairs recombination. It is noteworthy that bi-exponential fitting of STO/A-R TNTAs

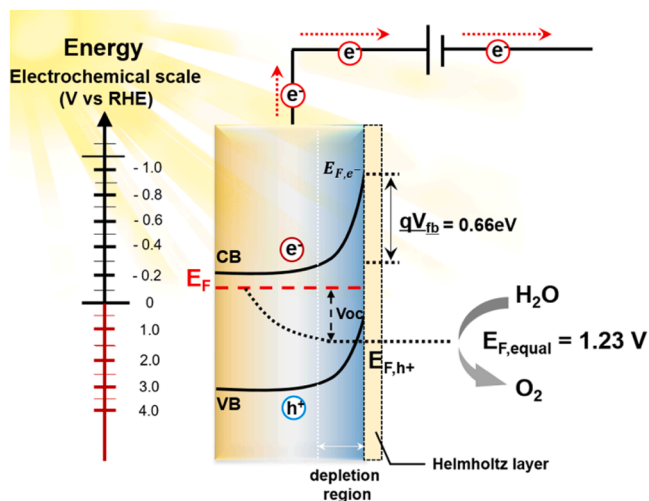


Fig. 4. The schematic diagram of calculated band alignment for STO/A-R TNTAs in a PAEC cell: $E_{F,e-}$ and $E_{F,h+}$ is the electron and hole quasi-Fermi level, respectively; V_{oc} : the voltage generated by the in-built junction under light illumination.

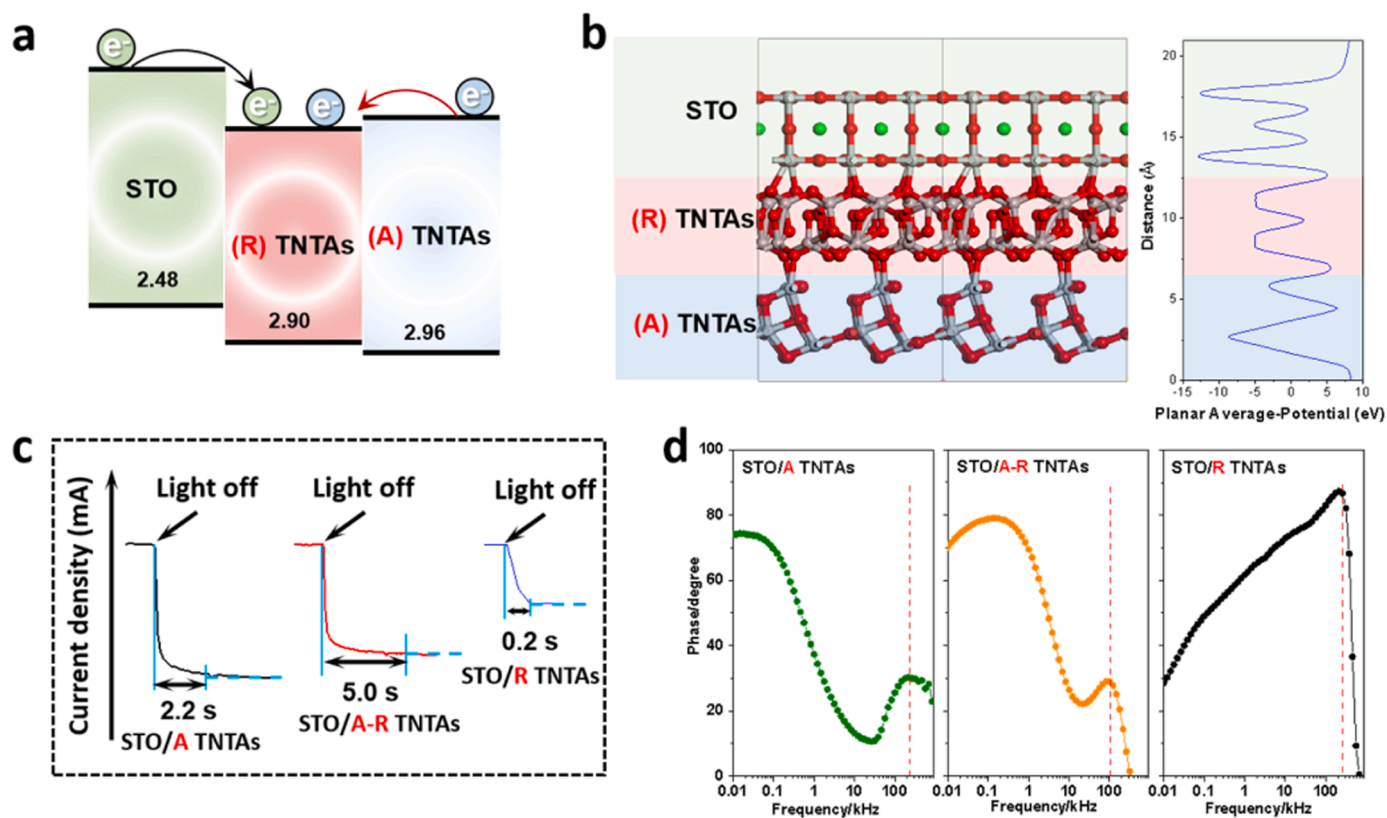
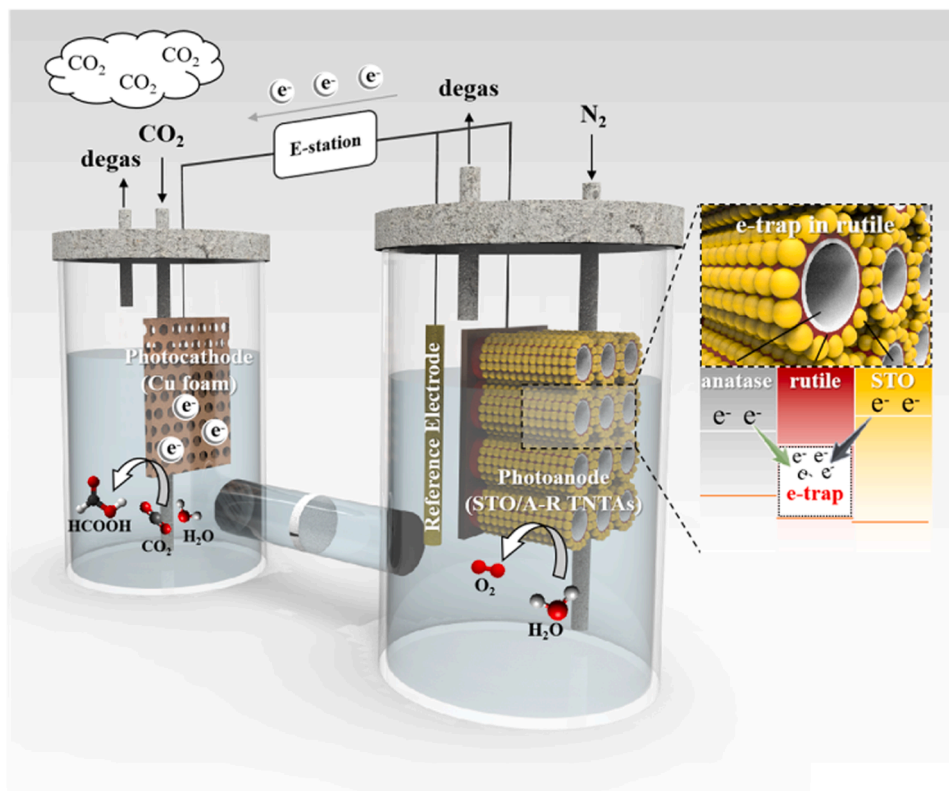


Fig. 5. (a) The mechanism of STO/A-R TNTAs binary junctions; (b) Calculated electrostatic potential difference at the STO/A-R TNTAs interface; (c) Amperometric i-t curves of as-prepared TNTAs-based photoanodes in N_2 -saturated electrolyte (0.5 M Na_2SO_4) at 0.5 V with a periodic light on/off. (d) Bode phase plots of EIS spectra.



Scheme 1. Schematic of the CO_2RR on the STO/A-R TNTAs photoanodes in the PAEC cell.

(with $\tau_1=10.22$ ns and $\tau_2=85.54$ ns) can be attributed to the free-electron recombination from CB to VB and stored electrons quenching, respectively. This observation demonstrates the presence of the electron storage process induced by the binary junctions within the STO/A-R TNTAs photoanode. Furthermore, both STO/A TNTAs and STO/R TNTAs exhibit a long-lived excited state, which is greater than that of pristine TiO_2 , thus indicating an improvement in CO_2RR . The electron storage in STO/A-R TNTAs effectively suppresses electron-hole recombination. The analysis of photoluminescence (PL) decay kinetics highlights the crucial role of the heterogeneous junction in enhancing electron storage and the heterophase junction in promoting electron storage.

4. Conclusion

In conclusion, our research has successfully optimized the band structure at the solid-liquid interface to establish binary junctions within the photoanode of STO/A-R TNTAs, thereby enhancing the photo-assisted electrocatalytic CO_2 reduction reaction. The introduction of a mixed-phase TiO_2 in the STO/A-R TNTAs enables *in-situ* electron storage, resulting in an augmented potential and prolonged lifetime of the photogenerated electrons. Consequently, the photoanode exhibits outstanding Faradic efficiency and selectivity for highly efficient conversion of CO_2 to HCOOH under simulated sunlight irradiation. This study introduces a viable *in-situ* electron storage strategy in SrTiO_3 and anatase-rutile TiO_2 binary junctions, which presents a novel approach to achieve photoreduction of CO_2 to high-value-added chemicals in a photoanode-driven PAEC system.

CRediT authorship contribution statement

Yingnan Cao: Writing – original draft, Methodology, Investigation, Formal analysis, Conceptualization. **Chi Zhang:** Investigation, Methodology, Writing – review & editing. **Wenchao Wang:** Writing – review & editing, Investigation, Funding acquisition, Conceptualization. **Yunni Liu:** Writing – review & editing, Investigation. **Ying Tao:** Writing – review & editing, Software, Investigation. **Jinchen Fan:** Writing – review & editing, Methodology. **Ming Chen:** Writing – review & editing, Resources. **Dieqing Zhang:** Writing – review & editing, Resources, Conceptualization. **Guisheng Li:** Writing – review & editing, Supervision, Resources, Funding acquisition, Conceptualization.

Declaration of Competing Interest

The authors declare that they have no known competing financial interests or personal relationships that could have appeared to influence the work reported in this paper.

Data availability

Data will be made available on request.

Acknowledgements

The authors thank the grants from the National Key Research and Development Program of China (2020YFA0211004), the National Natural Science Foundation of China (21876113, 22022608, 22306095, 21261140333), Shanghai Government (YDZX20213100003002), 111 Innovation and Talent Recruitment Base on Photo-chemical and Energy Materials (No. D18020), Environment and Conservation Fund (109/2022), Ministry of Education, and Shanghai Key Laboratory of Rare Earth Functional Materials, and Shanghai Engineering Research Center of Green Energy Chemical Engineering (18DZ2254200).

Appendix A. Supporting information

Supplementary data associated with this article can be found in the online version at doi:10.1016/j.apcatb.2024.123867.

References

- [1] Z. Jiang, X. Xu, Y. Ma, H. Cho, D. Ding, C. Wang, J. Wu, P. Oleynikov, M. Jia, J. Cheng, Y. Zhou, O. Terasaki, T. Peng, L. Zan, H. Deng, Filling metal-organic framework mesopores with TiO_2 for CO_2 photoreduction, *Nature* 586 (2020) 549–554, <https://doi.org/10.1038/s41586-020-2738-2>.
- [2] Y. Hu, F. Zhan, Q. Wang, Y. Sun, C. Yu, X. Zhao, H. Wang, R. Long, G. Zhang, C. Gao, W. Zhang, J. Jiang, Y. Tao, Y. Xiong, Tracking mechanistic pathway of photocatalytic CO_2 reaction at Ni sites using operando, time-resolved spectroscopy, *J. Am. Chem. Soc.* 142 (2020) 5618–5626, <https://doi.org/10.1021/jacs.9b12443>.
- [3] S. Wang, M. Xu, T. Peng, C. Zhang, T. Li, I. Hussain, J. Wang, B. Tan, Porous hypercrosslinked polymer- TiO_2 -graphene composite photocatalysts for visible-light-driven CO_2 conversion, *Nat. Commun.* 10 (2019) 676, <https://doi.org/10.1038/s41467-019-08651-x>.
- [4] X. Li, Y. Sun, J. Xu, Y. Shao, J. Wu, X. Xu, Y. Pan, H. Ju, J. Zhu, Y. Xie, Selective visible-light-driven photocatalytic CO_2 reduction to CH_4 mediated by atomically thin CuInS_2 layers, *Nat. Energy* 4 (2019) 690–699, <https://doi.org/10.1038/s41560-019-0431-1>.
- [5] F. Xu, K. Meng, B. Cheng, S. Wang, J. Xu, J. Yu, Unique S-scheme heterojunctions in self-assembled $\text{TiO}_2/\text{CsPbBr}_3$ hybrids for CO_2 photoreduction, *Nat. Commun.* 11 (2020) 4613, <https://doi.org/10.1038/s41467-020-18350-7>.
- [6] N. Nguyen, M. Xia, P.N. Duchesne, L. Wang, C. Mao, F.M. Ali, T. Yan, P. Li, Z. Lu, G. A. Ozin, Enhanced CO_2 photocatalysis by indium oxide hydroxide supported on TiN/TiO_2 nanotubes, *Nano Lett.* 21 (2021) 1311–1319, <https://doi.org/10.1021/acs.nanolett.0c04008>.
- [7] J. Zheng, S. Xu, J. Sun, J. Zhang, L. Sun, X. Pan, L. Li, G. Zhao, Boosting efficient C-N bonding toward photoelectrocatalytic urea synthesis from CO_2 and nitrate via close Cu/Ti bimetallic sites, *Appl. Catal. B Environ.* 338 (2023) 123056, <https://doi.org/10.1016/j.apcatb.2023.123056>.
- [8] D. Li, K. Yang, J. Lian, J. Yan, S. Liu, Powering the world with solar fuels from photoelectrochemical CO_2 reduction: basic principles and recent advances, *Adv. Energy Mater.* 12 (2022) 2201070, <https://doi.org/10.1002/aenm.202201070>.
- [9] F. Kuttassery, Y. Ohsaki, A. Thomas, R. Kamata, Y. Ebato, H. Kumagai, R. Nakazato, A. Sebastian, S. Mathew, H. Tachibana, O. Ishitani, H. Inoue, A molecular Z-scheme artificial photosynthetic system under the bias-free condition for CO_2 reduction coupled with two-electron water oxidation: photocatalytic production of CO/HCOOH and H_2O_2 , *Angew. Chem. Int. Ed.* 62 (2023) e202308956, <https://doi.org/10.1002/anie.202308956>.
- [10] H. Li, B. Zhu, B. Cheng, G. Luo, J. Xu, S. Cao, Single-atom Cu anchored on N-doped graphene/carbon nitride heterojunction for enhanced photocatalytic H_2O_2 production, *J. Mater. Sci. Technol.* 161 (2023) 192–200, <https://doi.org/10.1016/j.jmst.2023.03.039>.
- [11] Q. Zhu, Z. Deng, H. Xie, M. Xing, J. Zhang, Investigation of concerted proton-electron donors for promoting the selective production of HCOOH in CO_2 photoreduction, *ACS Catal.* 13 (2023) 3254–3262, <https://doi.org/10.1021/acscatal.3c00101>.
- [12] T. Ouyang, Y. Ye, C. Tan, S. Guo, S. Huang, R. Zhao, S. Zhao, Z. Liu, 1D $\alpha\text{-Fe}_2\text{O}_3/\text{ZnO}$ junction arrays modified by Bi as photocathode: high efficiency in photoelectrochemical reduction of CO_2 to HCOOH , *J. Phys. Chem. Lett.* 13 (2022) 6867–6874, <https://doi.org/10.1021/acs.jpclett.2c01509>.
- [13] J. Wang, J. Lee, J. Lee, T. Woo, Y. Zhang, W. Jiang, T. Kim, Regulating Cu atom orbital state on self-built photogate catalyst for improving HCOOH selectivity of CO_2 reduction, *Appl. Catal. B-Environ.* 324 (2023) 122287, <https://doi.org/10.1016/j.apcatb.2022.122287>.
- [14] J.J. Leung, J. Warnan, K.H. Ly, N. Heidary, D.H. Nam, M.F. Kuehnle, E. Reisner, Solar-driven reduction of aqueous CO_2 with a cobalt bis(terpyridine)-based photocathode, *Nat. Catal.* 2 (2019) 354–365, <https://doi.org/10.1038/s41929-019-0254-2>.
- [15] Y. Zhang, D. Pan, Y. Tao, H. Shang, D. Zhang, G. Li, H. Li, Photoelectrocatalytic reduction of CO_2 to syngas via SnO_x -enhanced Cu_2O nanowires photocathodes, *Adv. Funct. Mater.* 32 (2022) 2109600, <https://doi.org/10.1002/adfm.202109600>.
- [16] F. Wu, Y. Yu, H. Yang, L.N. German, Z. Li, J. Chen, W. Yang, L. Huang, W. Shi, L. Wang, X. Wang, Simultaneous enhancement of charge separation and hole transportation in a $\text{TiO}_2\text{-SrTiO}_3$ core-shell nanowire photoelectrochemical system, *Adv. Mater.* 29 (2017) 1701432, <https://doi.org/10.1002/adma.201701432>.
- [17] X. Tong, A.I. Channa, Y. You, P. Wei, X. Li, F. Lin, J. Wu, A. Vomiero, Z.M. Wang, Boosting the performance of eco-friendly quantum dots-based photoelectrochemical cells via effective surface passivation, *Nano Energy* 76 (2020) 105062, <https://doi.org/10.1016/j.nanoen.2020.105062>.
- [18] H. Rao, L.C. Schmidt, J. Bonin, M. Robert, Visible-light-driven methane formation from CO_2 with a molecular iron catalyst, *Nature* 548 (2017) 74–77, <https://doi.org/10.1038/nature23016>.
- [19] J.L. White, M.F. Baruch, J.E. Pander, Y. Hu, I.C. Fortmeyer, J.E. Park, T. Zhang, K. Liao, J. Gu, Y. Yan, T.W. Shaw, E. Abelev, A.B. Bocarsly, Light-driven heterogeneous reduction of carbon dioxide: photocatalysts and photoelectrodes, *Chem. Rev.* 115 (2015) 12888–12935, <https://doi.org/10.1021/acs.chemrev.5b00370>.

- [20] J. Zhang, R. Yin, Q. Shao, T. Zhu, X. Huang, Oxygen vacancies in amorphous InO_x nanoribbons enhance CO₂ adsorption and activation for CO₂ electroreduction, *Angew. Chem. Int. Ed.* 58 (2019) 5609–5613, <https://doi.org/10.1002/anie.201900167>.
- [21] M.M. Millet, G. Algara-Siller, S. Wrabetz, A. Mazheika, F. Girsig, D. Teschner, F. Seitz, A. Tarasov, S.V. Levchenko, R. Schlögl, E. Frei, Ni single atom catalysts for CO₂ activation, *J. Am. Chem. Soc.* 141 (2019) 2451–2461, <https://doi.org/10.1021/jacs.8b11729>.
- [22] C. Wang, Y. Zhao, H. Xu, Y. Li, Y. Wei, J. Liu, Z. Zhao, Efficient Z-scheme photocatalysts of ultrathin g-C₃N₄-wrapped Au/TiO₂-nanocrystals for enhanced visible-light-driven conversion of CO₂ with H₂O, *Appl. Catal. B Environ.* 263 (2020) 118314, <https://doi.org/10.1016/j.apcatb.2019.118314>.
- [23] S. Xu, Q. Shen, J. Zheng, Z. Wang, X. Pan, N. Yang, G. Zhao, Advances in biomimetic photoelectrocatalytic reduction of carbon dioxide, *Adv. Sci.* 9 (2022) 2203941, <https://doi.org/10.1002/adv.202203941>.
- [24] B. Shan, S. Vanka, T. Li, L. Troian-Gautier, M.K. Brennaman, Z. Mi, T.J. Meyer, Binary molecular-semiconductor p-n junctions for photoelectrocatalytic CO₂ reduction, *Nat. Energy* 4 (2019) 290–299, <https://doi.org/10.1038/s41560-019-0345-y>.
- [25] Z. Li, L. Luo, M. Li, W. Chen, Y. Liu, J. Yang, S. Xu, H. Zhou, L. Ma, M. Xu, X. Kong, H. Duan, Photoelectrocatalytic C-H halogenation over an oxygen vacancy-rich TiO₂ photoanode, *Nat. Commun.* 12 (2021) 6698, <https://doi.org/10.1038/s41467-021-26997-z>.
- [26] C. Liu, C. Zhang, G. Yin, T. Zhang, W. Wang, G. Ou, H. Jin, Z. Chen, A three-dimensional branched TiO₂ photoanode with an ultrathin Al₂O₃ passivation layer and a NiOOH cocatalyst toward photoelectrochemical water oxidation, *ACS Appl. Mater. Interfaces* 13 (2021) 13301–13310, <https://doi.org/10.1021/acsami.1c00948>.
- [27] R. Song, H. Chi, Q. Ma, D. Li, X. Wang, W. Gao, H. Wang, X. Wang, Z. Li, C. Li, Highly efficient degradation of persistent pollutants with 3D nanocone TiO₂-based photoelectrocatalysis, *J. Am. Chem. Soc.* 143 (2021) 13664–13674, <https://doi.org/10.1021/jacs.1c05008>.
- [28] X. Qian, Y. Zhang, Z. Wu, R. Zhang, X. Li, M. Wang, R. Che, Multi-path electron transfer in 1D double-shelled Sn@Mo₂C/C tubes with enhanced dielectric loss for boosting microwave absorption performance, *Small* 17 (2021) 2100283, <https://doi.org/10.1002/sml.202100283>.
- [29] J. Chen, X. Wu, Y. Gong, Y. Zhu, Z. Yang, B. Li, Q. Lu, Y. Yu, S. Han, Z. Zhang, Y. Zong, Y. Han, L. Gu, H. Zhang, Edge epitaxy of two-dimensional MoSe₂ and MoS₂ nanosheets on one-dimensional nanowires, *J. Am. Chem. Soc.* 139 (2017) 8653–8660, <https://doi.org/10.1021/jacs.7b03752>.
- [30] G. Li, Z. Lian, W. Wang, D. Zhang, H. Li, Nanotube-confinement induced size-controllable g-C₃N₄ quantum dots modified single-crystalline TiO₂ nanotube arrays for stable synergetic photoelectrocatalysis, *Nano Energy* 19 (2016) 446–454, <https://doi.org/10.1016/j.nanoen.2015.10.011>.
- [31] D. Kowalski, D. Kim, P. Schmuki, TiO₂ nanotubes, nanochannels and mesoporous: self-organized formation and applications, *Nano Today* 8 (2013) 235–264, <https://doi.org/10.1016/j.nantod.2013.04.010>.
- [32] J. Wu, Y. Tao, C. Zhang, Q. Zhu, D. Zhang, G. Li, Activation of chloride by oxygen vacancies-enriched TiO₂ photoanode for efficient photoelectrochemical treatment of persistent organic pollutants and simultaneous H₂ generation, *J. Hazard. Mater.* 443 (2023) 130363, <https://doi.org/10.1016/j.jhazmat.2022.130363>.
- [33] C. Ding, J. Shi, Z. Wang, C. Li, Photoelectrocatalytic water splitting: significance of cocatalysts, electrolyte, and interfaces, *ACS Catal.* 7 (2017) 675–688, <https://doi.org/10.1021/acscatal.6b03107>.
- [34] X. Zhou, R. Liu, K. Sun, Y. Chen, E. Verlage, S.A. Francis, N.S. Lewis, C. Xiang, Solar-driven reduction of 1 atm of CO₂ to formate at 10% energy-conversion efficiency by use of a TiO₂-protected III-V tandem photoanode in conjunction with a bipolar membrane and a Pd/C cathode, *ACS Energy Lett.* 1 (2016) 764–770, <https://doi.org/10.1021/acsenergylett.6b00317>.
- [35] Q. Wang, J. Cai, G.V. Biesold-McGee, J. Huang, Y.H. Ng, H. Sun, J. Wang, Y. Lai, Z. Lin, Silk fibroin-derived nitrogen-doped carbon quantum dots anchored on TiO₂ nanotube arrays for heterogeneous photocatalytic degradation and water splitting, *Nano Energy* 78 (2020) 105313, <https://doi.org/10.1016/j.nanoen.2020.105313>.
- [36] M. Radovic, N. Lampis, F.M. Granozio, P. Perna, Z. Ristic, M. Salluzzo, C. M. Schlepütz, U. Scotti di Uccio, Growth and characterization of stable SrO-terminated SrTiO₃ surfaces, *Appl. Phys. Lett.* 94 (2009) 022901, <https://doi.org/10.1063/1.3052606>.
- [37] C. Luo, J. Zhao, Y. Li, W. Zhao, Y. Zeng, C. Wang, Photocatalytic CO₂ reduction over SrTiO₃: correlation between surface structure and activity, *Appl. Surf. Sci.* 447 (2018) 627–635, <https://doi.org/10.1016/j.apsusc.2018.04.049>.
- [38] Y. He, L. Zhang, Y. Wei, X. Zhang, Z. Wang, R. Yu, Semicrystalline SrTiO₃-decorated anatase TiO₂ nanoparticle as heterostructure for efficient photocatalytic hydrogen evolution, *Small Methods* 6 (2022) 2101567, <https://doi.org/10.1002/smt.202101567>.
- [39] Y. Ou, J. Lu, W. Zhang, Q.U. Hassan, L. Zhu, J. Gao, X. Shi, Y. Huang, P. Liu, G. Zhu, In situ Sr²⁺ ions diffusion synthesis SrTiO_{3-x} quantum dots on TiO_{2-x} nanorods with efficient interfacial electron transfer for deeply NO oxidation removal, *Mater. Today Phys.* 27 (2022) 100804, <https://doi.org/10.1016/j.mtphys.2022.100804>.
- [40] C. Jiang, S.J.A. Moniz, A. Wang, T. Zhang, J. Tang, Photoelectrochemical devices for solar water splitting – materials and challenges, *Chem. Soc. Rev.* 46 (2017) 4645–4660, <https://doi.org/10.1039/C6CS00306K>.
- [41] J. Li, W. Su, J. Li, L. Wang, J. Ren, S. Zhang, P. Cheng, H. Hong, D. Wang, Y. Zhou, W. Mi, Y. Du, Orientational alignment of oxygen vacancies: electric-field-inducing conductive channels in TiO₂ film to boost photocatalytic conversion of CO₂ into CO, *Nano Lett.* 21 (2021) 5060–5067, <https://doi.org/10.1021/acs.nanolett.1c00897>.
- [42] S. Kim, W. Lee, C. An, D. Kwon, D. Kim, S. Cha, S. Cho, C. Hwang, Effect of growth temperature during the atomic layer deposition of the SrTiO₃ seed layer on the properties of RuO₂/SrTiO₃/Ru capacitors for dynamic random access memory applications, *ACS Appl. Mater. Interfaces* 10 (2018) 41544–41551, <https://doi.org/10.1021/acsami.8b17366>.
- [43] Y.V. Kolen'ko, A.A. Burukhin, B.R. Churagulov, N.N. Oleynikov, Synthesis of nanocrystalline TiO₂ powders from aqueous TiOSO₄ solutions under hydrothermal conditions, *Mater. Lett.* 57 (2003) 1124–1129, [https://doi.org/10.1016/S0167-577X\(02\)00943-6](https://doi.org/10.1016/S0167-577X(02)00943-6).
- [44] C. Huang, J. Fu, M. Xiang, J. Zhang, H. Zeng, X. Shao, Single-layer MoS₂ grown on atomically flat SrTiO₃ single crystal for enhanced trionic luminescence, *ACS Nano* 15 (2021) 8610–8620, <https://doi.org/10.1021/acsnano.1c00482>.
- [45] E. Guo, L. Yin, Tailored SrTiO₃/TiO₂ heterostructures for dye-sensitized solar cells with enhanced photoelectric conversion performance, *J. Mater. Chem. A* 3 (2015) 13390–13401, <https://doi.org/10.1039/C5TA02556G>.
- [46] Z. Yan, W. Wang, L. Du, J. Zhu, D.L. Phillips, J. Xu, Interpreting the enhanced photoactivities of 0D/1D heterojunctions of CdS quantum dots /TiO₂ nanotube arrays using femtosecond transient absorption spectroscopy, *Appl. Catal. B-Environ.* 275 (2020) 119151, <https://doi.org/10.1016/j.apcatb.2020.119151>.
- [47] E. Grabowska, M. Marchelek, T. Klimczuk, W. Lisowski, A. Zaleska-Medynska, TiO₂/SrTiO₃ and SrTiO₃ microspheres decorated with Rh, Ru or Pt nanoparticles: Highly UV–vis responsible photoactivity and mechanism, *J. Catal.* 350 (2017) 159–173, <https://doi.org/10.1016/j.jcat.2017.04.005>.
- [48] W. Guo, Y. Liu, Y. Sun, Y. Wang, W. Qin, B. Zhao, Z. Liang, L. Jiang, Vertical 3D printed forest-inspired hierarchical plasmonic superstructure for photocatalysis, *Adv. Funct. Mater.* 31 (2021) 2100768, <https://doi.org/10.1002/adfm.202100768>.
- [49] Y. Li, H. Wang, Q. Feng, G. Zhou, Z. Wang, Gold nanoparticles inlaid TiO₂ photoanodes: a superior candidate for high-efficiency dye-sensitized solar cells, *Energy Environ. Sci.* 6 (2013) 2156–2165, <https://doi.org/10.1039/C3EE23971C>.
- [50] W. Kim, T. Tachikawa, G. Moon, T. Majima, W. Choi, Molecular-level understanding of the photocatalytic activity difference between anatase and rutile nanoparticles, *Angew. Chem. Int. Ed.* 53 (2014) 14036–14041, <https://doi.org/10.1002/anie.201406625>.
- [51] J. Wang, T. Bo, B. Shao, Y. Zhang, L. Jia, X. Tan, W. Zhou, T. Yu, Effect of S vacancy in Cu₂SnS₄ on high selectivity and activity of photocatalytic CO₂ reduction, *Appl. Catal. B-Environ.* 297 (2021) 120498, <https://doi.org/10.1016/j.apcatb.2021.120498>.
- [52] L. Chen, Y. Xu, L. Su, T. He, L. Zhang, H. Shen, Q. Cheng, L. Liu, S. Bai, S.H. Hong, Visible-light-enhanced hydrogen evolution through anodic furfural electro-oxidation using nickel atomically dispersed copper nanoparticles, *Inorg. Chem.* 63 (2024) 730–738, <https://doi.org/10.1021/acs.inorgchem.3c03677>.
- [53] K. Ozawa, M. Emori, S. Yamamoto, R. Yukawa, S. Yamamoto, R. Hobara, K. Fujikawa, H. Sakama, I. Matsuda, Electron-hole recombination time at TiO₂ single-crystal surfaces: influence of surface band bending, *J. Phys. Chem. Lett.* 5 (2014) 1953–1957, <https://doi.org/10.1021/jz500770c>.
- [54] S. Dong, J. Hu, S. Xia, B. Wang, Z. Wang, T. Wang, W. Chen, Z. Ren, H. Fan, D. Dai, J. Cheng, X. Yang, C. Zhou, Origin of the adsorption-state-dependent photoactivity of methanol on TiO₂(110), *ACS Catal.* 11 (2021) 2620–2630, <https://doi.org/10.1021/acscatal.0c03930>.
- [55] J. Fujisawa, S. Kato, M. Hanaya, Interfacial charge-transfer transitions between TiO₂ nanoparticles and benzoic acid derivatives, *J. Phys. Chem. C* 125 (2021) 25075–25086, <https://doi.org/10.1021/acs.jpcc.1c07555>.
- [56] Z. Li, J. Feng, S. Yan, Z. Zou, Solar fuel production: strategies and new opportunities with nanostructures, *Nano Today* 10 (2015) 468–486, <https://doi.org/10.1016/j.nantod.2015.06.001>.
- [57] X. Chen, Y. Tang, W. Liu, Efficient Dye-sensitized solar cells based on nanoflower-like ZnO photoelectrode, *Molecules* 22 (2017) 1284, <https://doi.org/10.3390/molecules22081284>.